International Journal of Mechanical Sciences 176 (2020) 105548

Contents lists available at ScienceDirect

International Journal of Mechanical Sciences

journal homepage: www.elsevier.com/locate/ijmecsci

A semi-active metamaterial beam with electromagnetic quasi-zero-stiffness resonators for ultralow-frequency band gap tuning

Kai Wang [a,b], Jiaxi Zhou [a,b,*], Huajiang Ouyang [c], Li Cheng [d], Daolin Xu [a,b]

[a] State Key Laboratory of Advanced Design and Manufacturing for Vehicle Body, Hunan University, Changsha 410082, PR China
[b] College of Mechanical and Vehicle Engineering, Hunan University, Changsha 410082, PR China
[c] School of Engineering, University of Liverpool, Liverpool L69 3GH, UK
[d] Department of Mechanical Engineering, The Hong Kong Polytechnic University, Hong Kong, PR China

ARTICLE INFO

Keywords:
High-static-low-dynamic-stiffness
Locally resonant metamaterials
Semi-active resonator
Ultralow frequency
Tuneable band gap

ABSTRACT

Introducing a negative-stiffness mechanism (NSM) into a traditional linear resonator to form a high-static-low-dynamic-stiffness (HSLDS) resonator is an ideal way to create a low-frequency band gap. However, with the decrease in frequencies of the band gap, the band width narrows, which could hinder the application of the metamaterials for attenuating ultralow-frequency elastic waves. In this paper, a regulatory mechanism (RM) constituted by an electrically charged coil and a magnet ring is introduced into an HSLDS resonator to devise a semi-active quasi-zero-stiffness (QZS) resonator. With these semi-active resonators attached onto a beam periodically, a semi-active metamaterial beam (meta-beam) is realized. The expressions of both the restoring force and the stiffness of the semi-active resonator are derived firstly, and then the theoretical dispersion relation and the band structure are obtained by the transfer matrix method. Finally, by establishing and then numerically solving the equation of motion of the semi-active meta-beam, the wave transmissibility is acquired and utilized to validate the theoretically predicted band structure. The analytical and numerical results show that the band gap can be effectively tuned by the RM, which enables excellent wave manipulation in an ultralow and wide frequency range.

1. Introduction

Since its discovery in 2000 [1], the locally resonant phononic crystal (metamaterial) has received tremendous attention from researchers [1]. Prohibiting wave propagation in certain frequency ranges, referred to as stop bands or band gaps, such metamaterials have been widely applied in the fields of acoustic waveguide [2], wave manipulation [3] and vibration/noise control [4–9].

In previous investigations, various types of metamaterials, in one-dimension (1D) (including chains, rods, shafts and beams) [5,10–15], 2D [16–18]and 3D [19,20], have been designed theoretically, analysed numerically and validated experimentally. Compared with the Bragg Scattering band gap, the locally resonant band gap usually features a lower central frequency and a better wave attenuation within the band gap, conducive to low-frequency wave manipulation. However, most of the existing resonators, such as spring-mass devices [7,12,21,22], continuous beams [23], circular rubber-coated metal bars [24], rubber and metal rings [25] and piezoelectric patches [26], can hardly create ultralow-frequency band gaps since their resonant frequencies are not low enough. In addition, alongside the decrease in frequencies of the band gap is the decrease in its band width, which also hinders the further applications of metamaterials.

Much effort has been devoted to further reducing the band gap based on locally resonant mechanism. Zhang et al. [27] presented a metamaterial plate with periodic spiral resonators and successfully obtained low-frequency band gap (about 50 Hz). The achieved decrease in the band gap is attributed to the interaction between the local resonances and the traveling wave modes in the plate. Fang et al. [28] put forward a nonlinear chaotic mechanism to open a low-frequency band gap (about 40 Hz) in both 1D and 2D metamaterials. In the authors' early works [16,29,30], a negative-stiffness mechanism was introduced into the design of the resonator to construct a high-static-low-dynamic-stiffness (HSLDS) resonator with an ultralow resonant frequency. The results indicated that introducing the negative-stiffness mechanism is a promising way to open a band gap in an ultralowfrequency range (about 10 Hz).

Effort has also been made to overcome the limitation of the narrow bandwidth of a local resonant band gap. For example, Li et al. [31] presented a double-resonant phononic resonator; Fang et al. [32,33]

* Corresponding author at: College of Mechanical and Vehicle Engineering, Hunan University, Changsha 410082, PR China.
E-mail address: jxizhou@hnu.edu.cn (J. Zhou).

https://doi.org/10.1016/j.ijmecsci.2020.105548
Received 20 January 2020; Received in revised form 12 February 2020; Accepted 21 February 2020
Available online 24 February 2020

Designed a nonlinear resonator offering strong nonlinearity; Liu et al. [34] proposed resonant hierarchical lattice structures; Liu and Reina [34] designed hierarchical metamaterials and Celli et al. [35] proposed a rainbow metamaterial. In addition, by designing a unit cell including different types of resonators, a locally resonant band gap could also be broadened due to the coupling of multiple band gaps [36–38]. Coupling two resonant modes [12], and introducing an inertial amplification mechanism [39,40] were also shown to be alternative ways for broadening a band gap.

Apart from the passive mechanism, constructing an active or a semi-active resonator is another approach to lower the central frequency or broaden the bandwidth of a band gap [41]. Among active metamaterials, piezoelectric stacks [42–45] are usually used to realize the active control for a band gap. In addition, adjusting the mass [46,47] or the stiffness [48] with a semi-active method is also a promising way to tune a band gap.

The motivation of this paper is to propose an alternative method to overcome the limitation of the ultralow-frequency of the QZS resonator by introducing a regulatory mechanism (RM) (realized by a coil and a magnet ring), which opens a tuneable and wide low-frequency band gap in the ultralow-frequency range. The negative-stiffness mechanism (NSM) of the QZS resonator is composed of a pair of magnet rings to neutralize the stiffness of the linear resonator. Through periodic attachment of such resonators on a beam, a semi-active metamaterial beam, referred to as meta-beam, is devised. Based on the theoretical dispersion relation determined by the transfer matrix method, the band structures of both the QZS meta-beam and semi-active meta-beam are obtained, which are examined numerically in terms of the wave transmissibility through solving the equation of motion of the meta-beams.

This paper is organized as follows: In Section 2, both the physical and computational models of the meta-beam and the semi-active resonator are presented, alongside a static analysis of the resonator. The theoretical dispersion relations and the band structures are obtained through transfer matrix method in Section 3. In Section 4, numerical simulations and analyses of the semi-active meta-beam are conducted. Finally, conclusions are summarized in Section 5.

2. Modeling and static analysis of the meta-beam

2.1. Conceptual model

The physical and computational models of the semi-active meta-beam and the semi-active resonator are depicted in Fig. 1. As shown in Fig. 1(c) and (d), the semi-active resonator includes three parts, namely, a positive stiffness mechanism (PSM), a negative-stiffness mechanism (NSM) and a regulatory mechanism (RM). The PSM is a vertical spring, which not only provides a positive stiffness for the resonator, but also supports the mass of the resonator composed of inner magnetic rings of both the NSM and the RM. Note that, the mass of the resonator is installed onto a shaft with sliding bearing, which enables the motion of the resonator only in the vertical direction. The NSM is constituted by a pair of permanent magnet rings, used to neutralize the stiffness of the PSM. The RM is composed of an electrically charged coil and a permanent magnet ring, which is utilized to actively regulate the stiffness of the resonator. Attaching semi-active QZS resonators onto a thin beam by bolted joints, the semi-active meta-beam is constructed, as shown in Fig. 1(a).

2.2. Static analysis

The computational model of the RM is presented in Fig. 1(c). Based on the principle of magnetic field superposition and Ampere's current law, the permanent magnet ring is equivalent to two thin-walled solenoids which carry counter-flowing currents on the cylindrical surfaces, I_I for the inner solenoid and I_O for the outer one. Additionally, the static analysis of the semi-active QZS resonator is carried out with the aid of the filament method [49]. As presented in Fig. 2(a), both equivalent solenoids and the electrically charged coil are divided into several segments ($N_1 \times N_2$ for the coil, N_3 and N_4 for the inner and outer solenoids, respectively) according to the filament method. In Fig. 2(b), a pair of divided Maxwell's coils is highlighted which is utilized to derive the theoretical expression of the electromagnetic force of the RM.

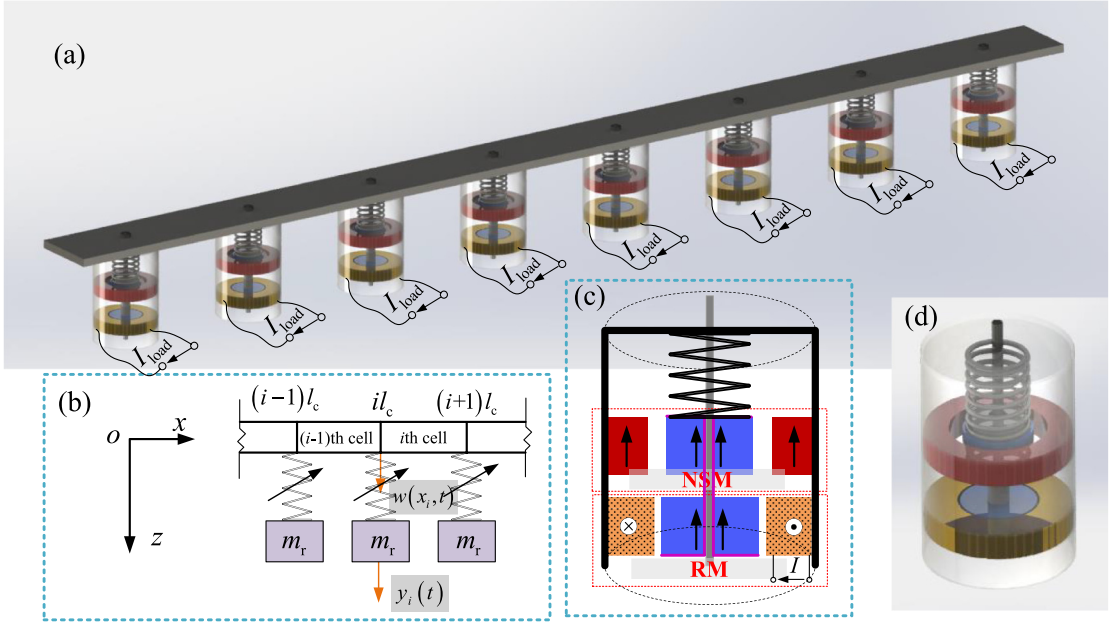

Fig. 1. (a) Physical model and (b) computational model of the semi-active QZS meta-beam, (c) schematic diagram of the static analysis, and (d) physical model of the semi-active resonator.

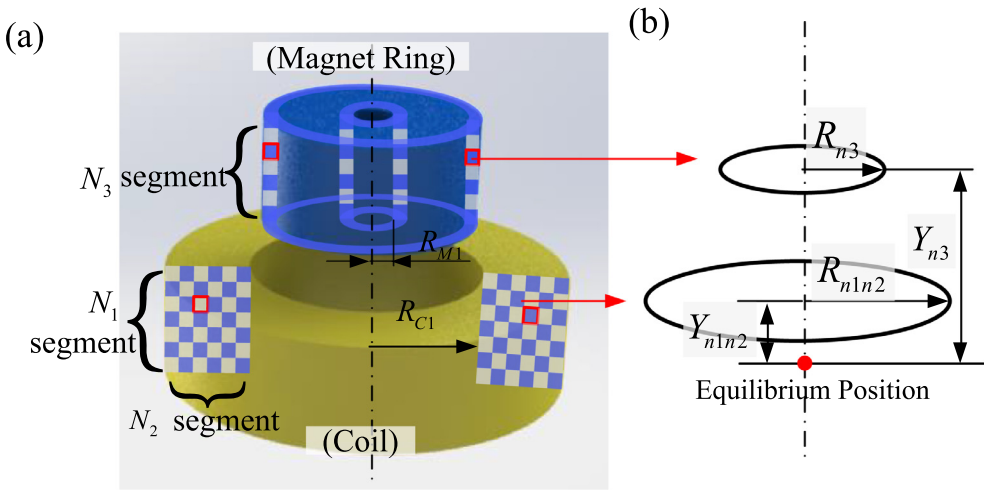

Fig. 2. (a) Division of both the charged coil and the permanent magnet ring of the RM into different meshes, and (b) a pair of Maxwell's coils.

Firstly, the currents of the thin-walled solenoids can be given by [50]

$$I_i = \begin{cases} \dfrac{JH}{\mu_0 N_3} \text{for} i = \text{I} \\ -\dfrac{JH}{\mu_0 N_3} \text{for} i = \text{O} \end{cases} \tag{1}$$

where J and H denote the polarization and the height of the permanent magnet ring, respectively; $\mu_0 = 4\pi \times 10^{-7}\text{N/A}^2$ is the vacuum permeability. For the highlighted Maxwell's coils shown in Fig. 2(b), the radii of the cells of the electrically charged coil and the equivalent outer solenoid of the permanent magnet ring can be written as

$$R_{n1n2} = R_{C1} + \left(n_2 - \frac{1}{2}\right)\frac{R_{C2} - R_{C1}}{N_2}, 0 < n_1 \le N_2 \tag{2}$$

$$R_{n3} = R_{M2} \tag{3}$$

where R_{C1} and R_{C2} are the inner and outer radii of the coil; N_2 the total number of the cells in the radial direction and R_{M1} the inner radii of the magnet ring. In the axial direction, the location of the Maxwell's coils can be given by

$$Y_{n1n2} = \left(n_1 - \frac{1}{2}\right)\frac{H}{N_1}, 0 < n_1 \le N_1 \tag{4}$$

$$Y_{n3} = y + \left(n_3 - \frac{1}{2}\right)\frac{H}{N_3}, 0 < n_3 \le N_3 \tag{5}$$

where N_1 is the number of the cells in the axial direction and y the moved displacement of the inner magnet ring with respect to the equilibrium position when an external excitation is applied on the resonator. Assuming the coil with a control current, the current in the filament writes

$$I_e = \frac{I_{\text{load}} \times N}{N_1 \times N_2} \tag{6}$$

where N and I_{load} denote the total turns of the insulating metal wire (yellow part in Fig. 2) and the load current, respectively. Note that, two assumptions [49,50], namely, currents of each filament being concentrated at the centres of the filaments and currents in charged coils being uniform, are introduced here to derive the current in the filament. With all of these parameters given above, the electromagnetic force between the Maxwell's coils can be obtained by

$$f_1(n_1, n_2, n_3, y) = \frac{\mu_0 I_e I_O (Y_{n3} - Y_{n1n2}) M_1}{2\sqrt{R_{n1n2} R_{n3}}(1 - M_1^2)} \left[(1 - M_1^2)K(M_1) - \frac{2 - M_1^2}{2}E(M_1)\right] \tag{7}$$

Following the same derivation procedure, the electromagnetic force between the Maxwell's coils formed by the filament of the charged coil and the filament of the inner solenoid can be expressed as

$$f_2(n_1, n_2, n_3, y) = \frac{\mu_0 I_e I_O (Y_{n4} - Y_{n1n2}) M_2}{2\sqrt{R_{n1n2} R_{n4}}(1 - M_2^2)} \left[(1 - M_2^2)K(M_2) - \frac{2 - M_2^2}{2}E(M_2)\right] \tag{8}$$

where Y_{n4} carry the same meaning as Y_{n3}. Note that, the functions K and E denote the second order Elliptic Integrals, which are given by

$$K(m) = \int_0^{\frac{\pi}{2}} \frac{\mathrm{d}\theta}{\sqrt{1 - m^2 \sin^2\theta}} \tag{9}$$

$$E(m) = \int_0^{\frac{\pi}{2}} \sqrt{1 - m^2 \sin^2\theta}\,\mathrm{d}\theta \tag{10}$$

Additionally, M_1 and M_2 are constants which are given by

$$M_1 = \sqrt{\frac{4R_{n1n2}R_{n3}}{(R_{n1n2} + R_{n3})^2 + (Y_{n3} - Y_{n1n2})}} \tag{11}$$

and

$$M_2 = \sqrt{\frac{4R_{n1n2}R_{n4}}{(R_{n1n2} + R_{n4})^2 + (Y_{n4} - Y_{n1n2})}} \tag{12}$$

Upon superposition of all the electromagnetic forces produced by Maxwell's coils, the electromagnetic force between the electrically charged coil and the permanent magnet ring can be given by

$$f_{\text{RM}} = \sum_{n_1}^{N_1}\sum_{n_2}^{N_2}\sum_{n_3}^{N_3} f_1(n_1, n_2, n_3, y) + \sum_{n_1}^{N_1}\sum_{n_2}^{N_2}\sum_{n_3}^{N_3} f_2(n_1, n_2, n_3, y) \tag{13}$$

For the NSM, the magnetic force between the inner and outer permanent magnet rings is given by Zhou et al. [51]

$$f_{\text{DM}} = \frac{\sigma^2(2r + 2l + g)}{\mu_0}[2\hbar(y) - \hbar(y + h) - \hbar(y + h)] \tag{14}$$

where $\sigma = \mathbf{J} \bullet \mathbf{n}$ is the magnetic pole surface density in which $\mathbf{J}$ and $\mathbf{n}$ denote the magnetic polarization vector and the unit normal vector, respectively; r, l, g and h are the inner radii of the inner magnet ring, the width of both the inner and outer magnet rings, the air gap between the inner and outer magnet ring, and the thickness of both the inner and outer magnet ring, respectively. In addition, the detailed expression of function $\hbar(a)$ can be given by

$$\hbar(a) = (2l + g)\arctan\left(\frac{2l + g}{a}\right) - 2(l + g)\arctan\left(\frac{l + g}{a}\right) + g\arctan\left(\frac{g}{a}\right) - \frac{a}{2}\left\{\ln\left[(2l + g)^2 + a^2\right] - 2\ln(l + g)^2 + \ln\left(g^2 + a^2\right)\right\} \tag{15}$$

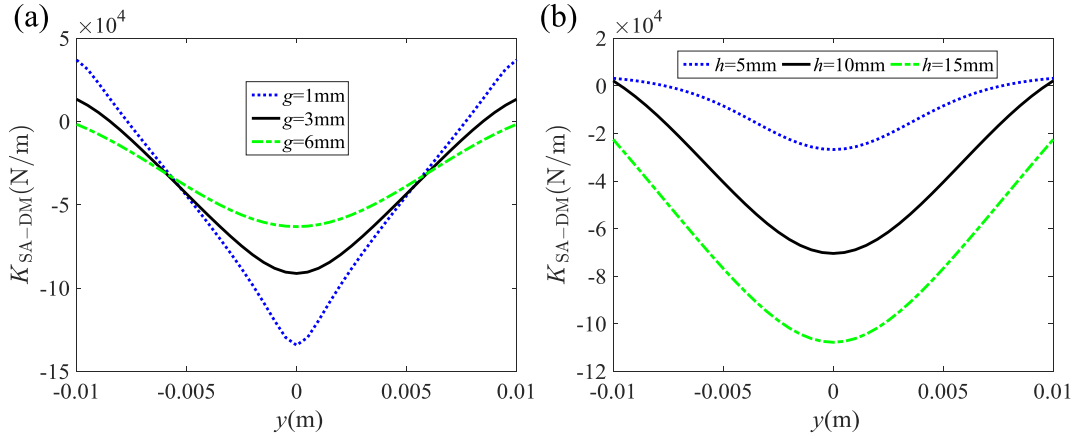

Fig. 3. Effect of (a) the air gap between the inner and outer magnet ring, and (b) the thickness of both the inner and outer magnet ring on the stiffness of the NSM.

For the RM and NSM, the directions of the restoring force are identical to that of the displacement y. Therefore, the restoring force of the semi-active QZS resonator can be written as

$$F_{\mathrm{SA-QZS}} = k_{\mathrm{v}} y - f_{\mathrm{RM}} - f_{\mathrm{DM}} \tag{16}$$

where k_{v} and y denote the stiffness of the vertical spring and the vertical displacement of the inner permanent magnet ring, respectively. Differentiating the restoring force $F_{\mathrm{SA\text{-}QZS}}$ with respect to displacement y yields the stiffness of the resonator as

$$K_{\mathrm{SA-QZS}} = k_{\mathrm{v}} - k_{\mathrm{DM}}(y) - \frac{\mathrm{d}f_{\mathrm{RM}}}{\mathrm{d}y} \tag{17}$$

where

$$k_{\mathrm{DM}}(y) = \frac{\sigma^2(2r+2l+g)}{2\mu_0}[2\lambda(y) - \lambda(y+h) - \lambda(y-h)] \tag{18}$$

in which

$$\lambda(a) = -\frac{2a^2}{a^2+(l+g)^2} - \frac{1}{2}\ln\left\{\frac{[(2l+g)^2+a^2](g^2+a^2)}{(l+g)^4}\right\} \tag{19}$$

Introducing a new variable $\gamma(y) = k_{\mathrm{DM}}(y)/k_{\mathrm{v}}$, named as stiffness ratio to evaluate the effect of the NSM, the stiffness of the semi-active resonator can be rewritten as

$$K_{\mathrm{SA-QZS}} = [1-\gamma(y)]k_{\mathrm{v}} - \mathrm{d}f_{\mathrm{RM}}/\mathrm{d}y \tag{20}$$

2.3. Static characteristics of the semi-active resonator

With parameters $\sigma = 1.35\mathrm{T}$, $r = 4\mathrm{mm}$, $g = 5\mathrm{mm}$, $l = 9\mathrm{mm}$, $h = 10\mathrm{mm}$, $J = 1.35\mathrm{T}$, $H = 10\mathrm{mm}$, $R_{M1} = 4\mathrm{mm}$, $R_{M2} = 14\mathrm{mm}$, $R_{C1} = 14.5\mathrm{mm}$, $R_{C2} = 24\mathrm{mm}$, $N_1 = 22$, $N_2 = 22$ and $N_3 = N_4 = 50$, the restoring force and the stiffness of the semi-active QZS resonator can be obtained according to Eqs. (16) and (17), as shown in Fig. 3(a) and (b), respectively.

The effect of the system parameters, including the air gap between the inner and outer magnet rings, and the thickness of both the inner and outer magnet rings, on the stiffness of the NSM is illustrated firstly in Fig. 3. It is evident that, with the decrease of the air gap, the negative stiffness of the NSM increases obviously, leading to a decrease in the stiffness of the resonator. Compared with the effect of the air gap, the thickness of the magnet rings has the opposite effect on the stiffness. As shown in Fig. 3(b), the stiffness of the NSM decreases obviously when the thickness of both the inner and outer magnet rings increases. Therefore, the stiffness of the resonator can be adjusted effectively by changing the parameters of the NSM, which provides a feasible way to design the resonators with different stiffness features.

The static features of the semi-active QZS resonator under different load currents are shown in Fig. 4. Firstly, considering a special case with no load current applied on the coil, the stiffness of the RM equals zero, and the semi-active resonator retreats to a traditional HSLDS resonator. As depicted by the black solid line in Fig. 4(b), the stiffness of the resonator can be neutralized effectively by the NSM. The stiffness of the QZS resonator equals the designated value at the equilibrium posi-

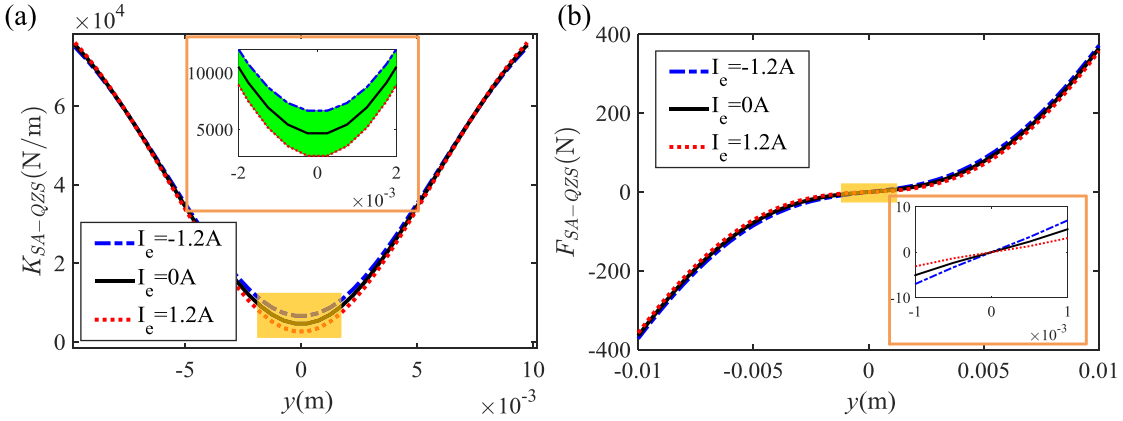

Fig. 4. (a) Restoring force and (b) the stiffness of the semi-active QZS resonator when the control current is −1.2 A (blue chain-dotted line), 0 A (black solid line) and 1.2 A (red dotted line), respectively. The green-shaded denotes the area of stiffness that can be controlled by adjusting the control current. (For interpretation of the references to color in this figure legend, the reader is referred to the web version of this article.)

tion ($y = 0$). When the resonator deviates from the equilibrium position with a small displacement, its stiffness is close to the designated value. Therefore, if there is no large external excitation applied on the traditional HSLDS resonator, it is reasonable that the nonlinear stiffness of the resonator is linearized as $[1 - \gamma(0)]k_v$, where $\gamma(0)$ denotes the ratio of the stiffness of the NSM at the equilibrium position to that of the PSM [52,53].

Once a load current is applied on the coil, the traditional HSLDS resonator becomes a semi-active one. As presented by the blue dotted line in Fig. 4, the stiffness of the semi-active resonator is larger than that of the HSLDS resonator at the equilibrium position when the load current is −1.2 A. Nevertheless, with the increase of the displacement, the difference between the stiffness of the semi-active resonator and that of the HSLDS resonator gradually reduces. In contrast, the stiffness of the semi-active resonator is smaller than that of the HSLDS resonator when the load current is 1.2 A. The controllable range of the stiffness of the semi-active resonator is highlighted by the green shaded area in Fig. 4(b), within which the stiffness can be tuned easily by adjusting the value or the direction of the load current.

Additionally, as illustrated in Fig. 4(a) and (b), the stiffness feature of the semi-active resonator is similar to that of the HSLDS resonator. Therefore, if the excitation amplitude is small enough, the nonlinear stiffness of the semi-active resonator can be linearized as

$$K^{A}_{SA-QZS} = [1 - \gamma(0)]k_v - \mathrm{d}f_{RM}/\mathrm{d}y|_{y=0} \tag{21}$$

where $\mathrm{d}f_{RM}/\mathrm{d}y|_{y=0}$ denotes the stiffness of the RM at the equilibrium position. The linearized stiffness will be utilized in the analytical analysis of the semi-active meta-beam for band structures.

3. Wave dispersion on meta-beam

In this section, wave dispersion on the semi-active meta-beam is derived by utilizing the transfer matrix method. According to the dispersion relation, band structures of both the passive HSLDS meta-beam and the semi-active QZS meta-beam are determined.

3.1. Dispersion relation

In order to obtain the theoretical band structures of the meta-beam with semi-active QZS resonators, an infinite beam with an infinite number of resonators is considered firstly. For the host beam, the equation of motion can be written as [37]

$$EI\frac{\partial^4 w(x,t)}{\partial x^4} + \rho S\frac{\partial^2 w(x,t)}{\partial t^2} = 0 \tag{22}$$

where $w(x, t)$ is the transverse deflection of the beam at point x; E, I, S and ρ the Young's modulus, the second moment of area, the cross-sectional area and the density of the host beam, respectively. The conventional small displacement assumption is adopted. Upon linearizing the stiffness of the semi-active QZS resonator at the equilibrium position, the equation of motion of the jth semi-active QZS can be given by

$$m_r\ddot{y}_j(t) - \left\{k_v[1 - \gamma(0)] - \mathrm{d}f_{RM}/\mathrm{d}y|_{y=0}\right\}\left[w(x_j,t) - y_j(t)\right] = 0 \tag{23}$$

Assuming that the transverse deflection of the beam at point x as

$$w(x) = W(x)e^{i\omega t} \tag{24}$$

where $W(x) = \Delta\Phi(x)^T$ denotes the mode shape function of the host beam in which

$$\begin{cases} \mathbf{\Delta} = \{A \quad B \quad C \quad D\} \\ \Phi(x) = \{\cos(\nu x) \quad \sin(\nu x) \quad \cosh(\nu x) \quad \sinh(\nu x)\} \end{cases} \tag{25}$$

with A, B, C, D being unknown parameters and ω the angular frequency. In the jth unit cell where $x' = x - jl_c$ and $jl_c \le x \le (j-1)l_c$, the mode function can be written as $W_j(x') = \Delta_j\Phi(x')^T$ where $\Delta_j = \{A_j \quad B_j \quad C_j \quad D_j\}$.

Note that the parameter $\nu = \sqrt[4]{\rho S\omega^2/EI}$ is the wavenumber. By using the continuities of displacement, slope, bending moment and shear force at the attaching point of the jth resonator, and employing the Floquet-Bloch theorem $\mathbf{\Delta}_j = e^{iql_c}\mathbf{\Delta}_{j-1}$ and the transfer matrix method [29], one can easily obtain the dispersion relation of the semi-active meta-beam as

$$\left|\mathbf{G}^{-1}\mathbf{H} - e^{iql_c}\mathbf{I}\right| = 0 \tag{26}$$

where $\mathbf{I}$, q, l_c denote a 4×4 identity matrix, the bending wave vector and the lattice constant, respectively, and

$$\mathbf{G} = \begin{bmatrix} 1 & 0 & 1 & 0 \\ 0 & \nu & 0 & \nu \\ -\nu^2 & 0 & \nu^2 & 0 \\ -\frac{K^{A}_{SA-QZS}m_r\omega^2}{K^{A}_{SA-QZS}-m_r\omega^2} & -EI\nu^3 & -\frac{K^{A}_{SA-QZS}m_r\omega^2}{K^{A}_{SA-QZS}-m_r\omega^2} & EI\nu^3 \end{bmatrix} \tag{27}$$

$$H = \begin{bmatrix} \cos(\nu l_c) & \sin(\nu l_c) & \cosh(\nu l_c) & \sinh(\nu l_c) \\ -\beta\sin(\nu l_c) & \beta\cos(\nu l_c) & \beta\sinh(\nu l_c) & \beta\cosh(\nu l_c) \\ -\beta^2\cos(\nu l_c) & -\beta^2\sin(\nu l_c) & \beta^2\cosh(\nu l_c) & \beta^2\sinh(\nu l_c) \\ EI\beta^3\sin(\nu l_c) & -EI\beta^3\cos(\nu l_c) & EI\beta^3\sinh(\nu l_c) & EI\beta^3\cosh(\nu l_c) \end{bmatrix} \tag{28}$$

For a given frequency, one can obtain the solution of the wave vector according to the dispersion relation.

3.2. The band structure of the passive HSLDS meta-beam

In order to emphasize the improvement of the semi-active QZS resonator over the traditional HSLDS resonator in tuning and broadening the low-frequency band gap, some parameters of the semi-active QZS meta-beam are selected from Ref. [29]. All the geometrical and material parameters are listed as:E = 70Gpa, ρ = 2700kg/m^3, $I = 5.968 \times 10^{-9}$m^4, $S = 1.602 \times 10^{-4}$m^{-2}, l_c = 0.125m, m_r = 0.0482kg and $k_v = 7.5 \times 10^4$N/m. The effect of the stiffness ratio $\gamma(0)$ on the band structure is illustrated in Fig. 5 when the load current is zero and the semi-active resonator degenerates into a traditional HSLDS one. In each subplot, the left-panel and the right-panel denote the imaginary part and real part of ql_c/π, respectively. The shaded areas indicate the band gap. Clearly, both the imaginary and real parts can predict the width and location of the band gap, while the imaginary part also illustrates the wave attenuation feature within the band gap.

For the case of $\gamma(0) = 0$, as delineated in Fig. 6(a), the semi-active QZS resonator degenerates into a linear one and the band gap locates at a high-frequency range around 200 Hz. By adjusting the parameters of the NSM to increase the value of $\gamma(0)$, as shown in Fig. 5(b)–(d), the band gap is shifted to low-frequency. For example, the band gap centered at is 140 Hz when $\gamma(0) = 0.5$ is shifted to 19 Hz when $\gamma(0) = 0.99$ through introducing the NSM. Actually, the reduction of the central frequency induced by the NSM can be explained by the variation of the stiffness of the HSLDS resonator. With the increase of the stiffness ratio, the stiffness of the resonator is effectively neutralized by the NSM, causing a lower resonant frequency and thus the reduction in the central frequency.

3.3. The band structure of the semi-active QZS meta-beam

When a current is loaded on the coil, the HSLDS resonator becomes a semi-active one, leading to a semi-active meta-beam empowered with tuning capability. Its corresponding band structure is computed and presented in Fig. 6, where different shadowed areas denote different band gaps: the original band gap, extended band gap by load current and the entire band gap, respectively. For $\gamma(0) = 0.95$, as shown in Fig. 6(a), the band gap of the beta-beam is significantly altered. As illustrated in Fig. 6(a), the band gap moves to a high frequency range for a load current −1.2 A (the maximum allowable current to be loaded). This is plausible since the load current leads to a weakening of the negative stiffness and then results in an increase of the resonant frequency. In contrast,

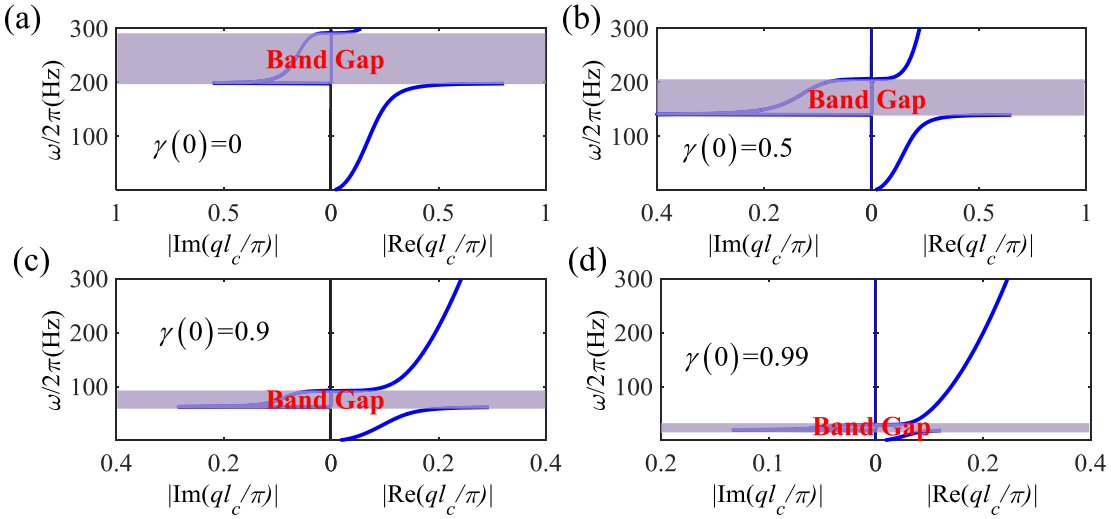

Fig. 5. Theoretical band gaps of the meta-beam with traditional HSLDS resonators when (a) $\gamma(0) = 0$, (b) $\gamma(0) = 0.5$, (c) $\gamma(0) = 0.9$ and (d) $\gamma(0) = 0.99$. The shaded areas show the band gap where the flexural wave is suppressed along the meta-beam.

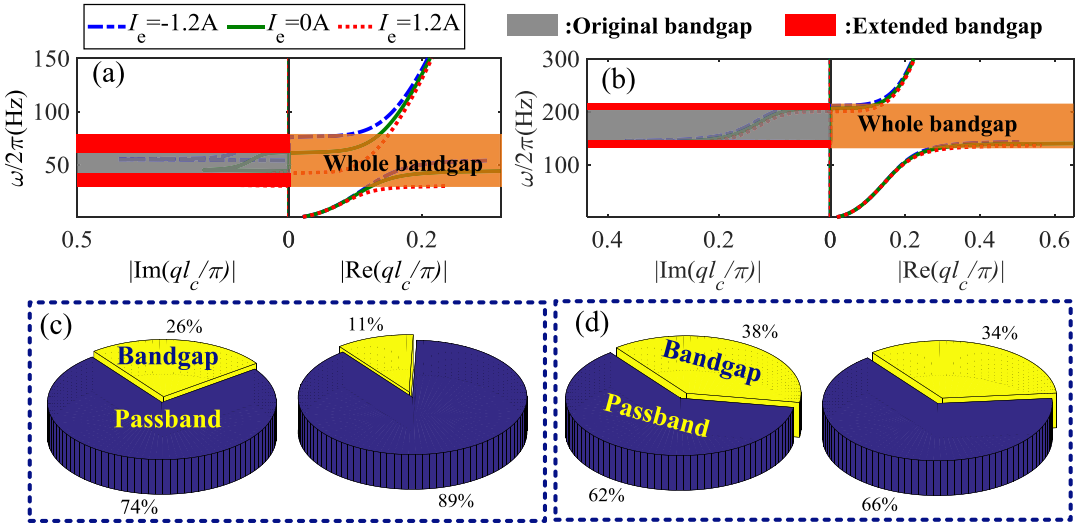

Fig. 6. Effect of load current on the band gap when (a) $\gamma(0) = 0.95$ and (b) $\gamma(0) = 0.5$. The bandwidth ratio of the original bandgap to the frequency range of (0–300 Hz), and the ratio of the extended bandgap to the frequency range of (0–300 Hz) when (c) $\gamma(0) = 0.95$ and (d) $\gamma(0) = 0.5$.

the band gap moves to a low frequency range when the load current is 1.2 A. Similarly, the reduction of the central frequency of the band gap can also be attributed to the enhancement of the negative stiffness caused by the positive load current.

When the negative-stiffness ratio is $\gamma(0) = 0.5$, the effect of load current on the band gap of the semi-active meta-beam is illustrated in Fig. 6(b). Clearly, the band gap moves to a high frequency range when a negative current is applied on the coil, while it shifts to a low frequency range for a positive load current. The band gap exhibits the same variation trend when $\gamma(0) = 0.05$.

To further illustrate the effect of load current on the band gap, Fig. 6(c) and (d) show the bandwidth ratio of the band gap to the given frequency range (0–300 Hz), when the stiffness ratio is 0.95 and 0.5, respectively. As shown in Fig. 6(c), the RM obviously affects the bandwidth when $\gamma(0) = 0.95$, leading to a broadening of the band gap from 7% to 16% (more than twice) by tuning the load current. However, when $\gamma(0) = 0.5$, the RM has less effect on the semi-active resonator, resulting in an slight enlargement of the band gap from 19% to 21%. Therefore, introducing the RM into the HSLDS resonator is an effective approach to broaden the band gap in the ultralow frequency range.

The impact of the stiffness ratio on the lower and upper frequencies of the band gap is shown in Fig. 7(a). It is evident that with the increase of the stiffness ratio, both the lower and upper frequencies are reduced, leading to a lower but narrower band gap for both the HSLDS and the semi-active resonators. However, as depicted in Fig. 7(a), the band gap created by the latter is broader than that of the former, more obvious with the increase of the stiffness ratio, which is in line with the tendency observed in Fig. 6. To quantify this, a parameter ε named as amplification coefficient is defined as

$$\varepsilon = \frac{(\omega_{\mathrm{EEF}} - \omega_{\mathrm{EBF}}) - (\omega_{\mathrm{OEF}} - \omega_{\mathrm{OBF}})}{\omega_{\mathrm{OEF}} - \omega_{\mathrm{OBF}}} \tag{29}$$

where subscripts 'EEF' and 'EBF' denote the upper and lower frequencies of the extended band gap, and 'OEF' and 'OBF' denote their counterparts of the original band gap, respectively As shown in Fig. 7(b), with the increase of the negative-stiffness ratio, ε increases firstly gently and then rapidly, evidencing the pivotal role that RM plays in broadening the bandwidth in the low, especially ultralow frequency range, and alleviating the drawbacks of the traditional HSLDS resonator.

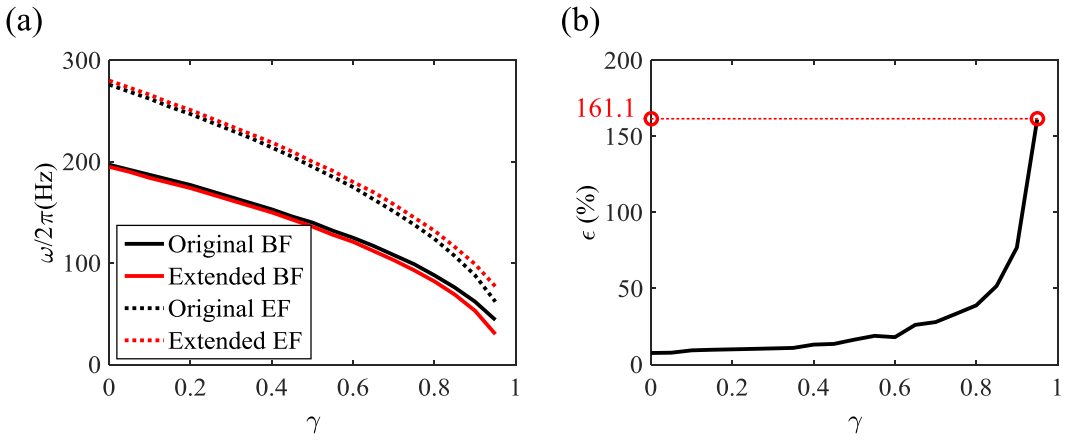

Fig. 7. (a) Lower and upper frequencies of the band gap for different negative-stiffness ratios. (b) The amplification coefficient of the band gap for different negative-stiffness ratios.

4. Numerical simulations for wave transmissibility

4.1. Numerical simulations

In this section, the wave transmissibility of a meta-beam with a finite length and a free-free boundary condition under an external excitation applied on the left-hand side ($y = 0$) is investigated with the Galerkin method. This section commences with verifying the effect of the NSM (HSLDS resonator) on the wave transmissibility, and then assesses the adjustment of the band gap by the RM (semi-active resonator).

The equation of the motion of the coupled meta-beam with HSLDS resonators is given by

$$EI\frac{\partial^4 w(x,t)}{\partial w^4}+\rho S\frac{\partial^2 w(x,t)}{\partial t^2}=f(t)\delta(x-0)+\sum_{j=1}^{n}F_{\mathrm{SA-QZS}}\left(x_j,t\right)\delta\left(x-x_j\right) \tag{30}$$

where

$$\begin{aligned}F_{\mathrm{DM}}\left(x_j,t\right)&=k_{\mathrm{v}}\left[z_j(t)-w\left(x_j,t\right)\right]\\&-\frac{\sigma^2(2r+2l+g)}{2\mu_0}\left[2\hbar\left(z_j(t)-w\left(x_j,t\right)\right)\right.\\&\left.-\hbar\left(z_j(t)-w\left(x_j,t\right)+h\right)-\hbar\left(z_j(t)-w\left(x_j,t\right)+h\right)\right]\end{aligned} \tag{31}$$

denotes the restoring force of the jth resonator.

Employing the Galerkin method to discretize the system, the transverse deflection of the host beam is postulated as

$$w(x,t)=\sum_{k=1}^{K}\phi_k(x)p_k(t) \tag{32}$$

in which $\varphi_k(x)$ and $p_k(t)$ denote the trial function and the generalized displacement, respectively. The trial function of the beam is given by

$$\begin{aligned}\phi_k(x)=&\sin\left(\beta_k x\right)+\sinh\left(\beta_k x\right)+\frac{\sin\left(\beta_k x\right)-\sinh\left(\beta_k x\right)}{\cosh\left(\beta_k x\right)-\cos\left(\beta_k x\right)}\\&\left[\cosh\left(\beta_k x\right)+\cos\left(\beta_k x\right)\right]\end{aligned} \tag{33}$$

where β_k is the wavenumber of the Euler-Bernoulli beam, which can be acquired by solving the characteristic equation $\cos(\beta_k L)\cosh(\beta_k L) = 1$. Inserting (32) into the equation of motion of the coupled meta-beam (Eq. (30)), one can obtain

$$\begin{aligned}&\sum_{k}^{K}\left[EI\phi_k^{(4)}(x)p_k(t)+\rho S\phi_k(x)\ddot{p}_k(t)\right]=f(t)\delta(x-0)\\&+\sum_{j=1}^{n}F_{\mathrm{SA-QZS}}\left(x_j,t\right)\delta\left(x-x_j\right)\end{aligned} \tag{34}$$

where

$$\begin{aligned}F_{\mathrm{SA-QZS}}\left(x_j,t\right)&=k_{\mathrm{v}}\left[z_j(t)-w\left(x_j,t\right)\right]\\&-\frac{\sigma^2(2r+2l+g)}{2\mu_0}\left[2\hbar\left(z_j(t)-\sum_{k=1}^{K}\phi_k\left(x_j\right)p_k(t)\right)\right.\\&-\hbar\left(z_j(t)-\sum_{k=1}^{K}\phi_k\left(x_j\right)p_k(t)+h\right)-\left.\hbar\left(z_j(t)-\sum_{k=1}^{K}\phi_k\left(x_j\right)p_k(t)+h\right)\right]\end{aligned} \tag{35}$$

Introducing a weight function $\phi_k(x)$ that is identical to the trial function, and multiplying Eq. (34) with $\phi_k(x)$ and then integrating along the whole meta-beam from 0 to L, one can obtain the following equation

$$\begin{aligned}&EI\sum_{k}^{K}\int_0^L\phi_k^{(4)}(x)\varphi_k(x)p_k(t)\mathrm{d}x+\rho S\sum_{k}^{K}\int_0^L\phi_k(x)\varphi_k(x)\ddot{p}_k(t)\mathrm{d}x\\&=\int_0^L f(t)\delta(x-0)\varphi_k(x)\mathrm{d}x+\sum_{j=1}^{n}\int_0^L\varphi_k(x)F_{\mathrm{SA-QZS}}\left(x_j,t\right)\delta\left(x-x_j\right)\mathrm{d}x\end{aligned} \tag{36}$$

For the jth HSLDS resonator with damping, the equation of motion can be given by

$$m_{\mathrm{r}}\ddot{z}_j+2\zeta_{\mathrm{r}}\sqrt{m_{\mathrm{r}}k_{\mathrm{v}}}\left[\dot{z}(t)-\sum_{k=1}^{K}\phi_k\left(x_j\right)\dot{p}_k(t)\right]+F_{\mathrm{SA-QZS}}\left(x_j,t\right)=0 \tag{37}$$

Owing to the orthogonality of the mode functions of the host beam and considering the modal damping, Eq. (36) can be rewritten as

$$\begin{aligned}&\left[\rho S\int_0^L\phi_k^2(x)\mathrm{d}x\right]\ddot{p}_k+\left[2\zeta_k\sqrt{\rho S\int_0^L\phi_k^2(x)\mathrm{d}x\cdot EI\int_0^L\phi_k^{(4)}(x)\phi_k(x)\mathrm{d}x}\right]\dot{p}_k\\&+\left[EI\int_0^L\phi_k^{(4)}(x)\phi_k(x)\mathrm{d}x\right]p_k\\&=\phi_k(0)f(t)+2\zeta_{\mathrm{r}}\sqrt{m_{\mathrm{r}}k_{\mathrm{v}}}\sum_{j=1}^{n}\phi_k\left(x_j\right)\left[\dot{z}(t)-\sum_{s=1}^{S}\phi_k\left(x_j\right)\dot{p}_k(t)\right]\\&+\sum_{j=1}^{n}\phi_k\left(x_j\right)F_{\mathrm{SA-QZS}}\left(x_j,t\right)\end{aligned} \tag{38}$$

Note that Eq. (38) is an ordinary differential equation which can be written in the following simple form

$$M_{\mathrm{eq},k}\ddot{p}_k+C_{\mathrm{eq},k}\dot{p}_k+K_{\mathrm{eq},k}p_k=F_{\mathrm{eq},k} \tag{39}$$

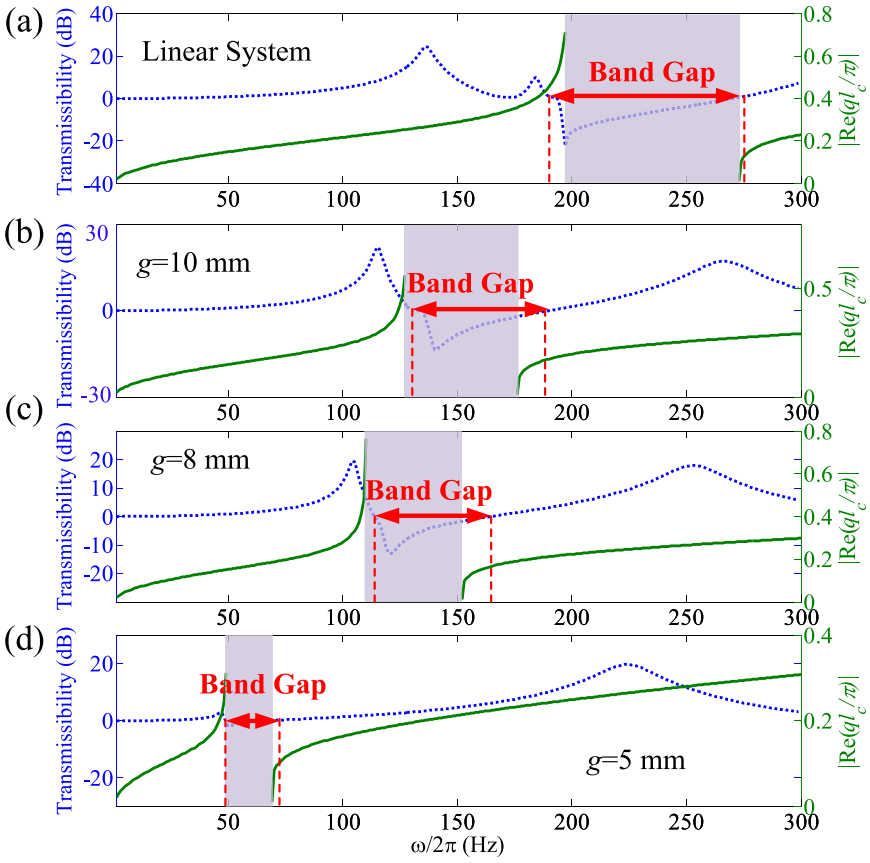

Fig. 8. Comparison between the analytical band structure (left-hand axle) and the wave transmissibility (right-hand axle) when the external exciting amplitude is F = 1 N. (a) Linear system, (b) g = 10 mm, (c) g = 8 mm and (d) g = 5 mm. The shaded areas denote the band gap calculated by transfer matrix method, and the red lines with arrows represent the band gap obtained by numerical simulations. (For interpretation of the references to color in this figure legend, the reader is referred to the web version of this article.)

where

$$
\begin{aligned}
M_{\mathrm{eq},k} &= \rho S \int_0^L \phi_k^2(x)\mathrm{d}x \\
C_{\mathrm{eq},k} &= 2\zeta_k \sqrt{\rho S \int_0^L \phi_k^2(x)\mathrm{d}x \cdot EI \int_0^L \phi_k^{(4)}(x)\phi_k(x)\mathrm{d}x} \\
K_{\mathrm{eq},k} &= EI \int_0^L \phi_k^{(4)}(x)\phi_k(x)\mathrm{d}x \\
F_{\mathrm{eq},k} &= \phi_k(0) f(t) + 2\zeta_{\mathrm{r}} \sqrt{m_{\mathrm{r}} k_{\mathrm{v}}} \sum_{j=1}^{n} \phi_k(x_j) \left[\dot{z}(t) - \sum_{j=1}^{N} \phi_k(x_j) \dot{p}_k(t) \right] \\
&\quad + \sum_{j=1}^{n} \phi_k(x_j) F_{\mathrm{SA-QZS}}(x_j, t)
\end{aligned}
\tag{40}
$$

For a given frequency, one can obtain the generalized displacement by solving Eqs. (37) and (39). Substituting the generalized displacement into Eq. (32), the wave propagation in the finite-length meta-beam (including 8 unit cells) can be estimated. Additionally, the number of Galerkin trial functions K should be large enough to satisfy the requirement on computational accuracy.

4.2. Verification of the band structures

With parameters $\zeta_k = 0.05$, $\zeta_{\mathrm{r}} = 0.01$,$g = 5 \times 10^{-3}$m and $K = 12$, the wave transmissibility in the meta-beam and the real part of ql_{c}/π are displayed in Fig. 8 for different air gaps between the inner and outer magnet rings. In this figure, the wave transmissibility is defined as the ratio between the left-hand and right-hand displacement response, namely, $20\log||w_{\mathrm{L}}(\omega)/w_{\mathrm{R}}(\omega)||$, which is utilized to estimate the propagation characteristics of the flexural wave alone the meta-beam. The blue dotted line and green solid line show the wave transmissibility and the real part of ql_{c}/π, respectively. The shaded areas represent the numerical band gap, where the flexural wave is suppressed when it propagates along the meta-beam, and the frequency ranges surrounded by the red dashed lines show the band gaps obtained by the analytical analysis by using the linearized stiffness.

Comparing the numerical with analytical results shows a good agreement between them, which verify the rationality of the linearization on the nonlinear stiffness. However, since the damping is neglected in the theoretical analysis, whether the resonator is linear (Fig. 8(a)) or HSLDS (Fig. 8(b)–(d)), the width of the numerically calculated band gap is always larger than that of the theoretical one. More importantly, the location of the band gap generated by HSLDS resonators is lower than that by linear ones. Additionally, with the decrease of the air gap between the inner and outer magnet rings, the central frequency of the band gap decreases further, which is in line with the analytical prediction presented in Fig. 5.

4.3. Wave transmissibility of the semi-active meta-beam

For the semi-active meta-beam, a load current is applied on the coil, and the neutralization of stiffness is achieved by both the NSM and the RM. However, as shown in Eq. (13), the expression of the electromagnetic force between the coil and the permanent magnet ring is complicated, and the numerical simulation of wave propagation along the semi-active meta-beam is difficult. In order to carry out the dynamic analysis, the complicated nonlinear expression is approximated as a polynomial through Taylor expansion. However, with the increase of the displacement, the error between the exact expression and the approximated one increases notably [51]. Therefore, in the current analysis, the polynomial fitting method is employed to approximate the tedious expression of the electromagnetic force as a polynomial with components up to order seven. Then, the restoring force of the jth resonator can be

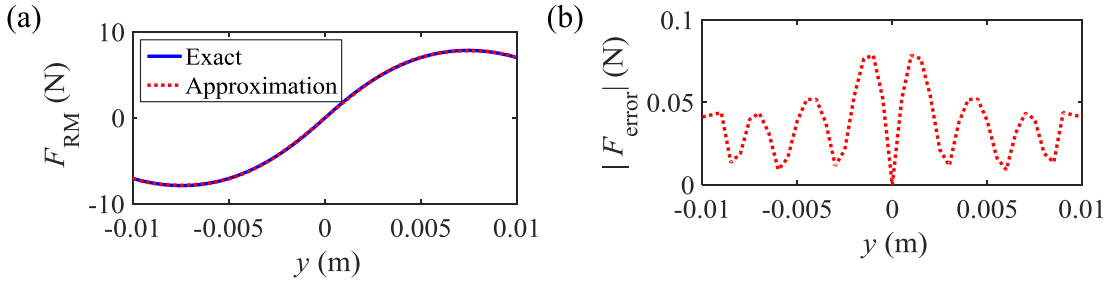

Fig. 9. (a) The exact and approximate electromagnetic force, and (b) the fitted error when the load current is 1.2 A.

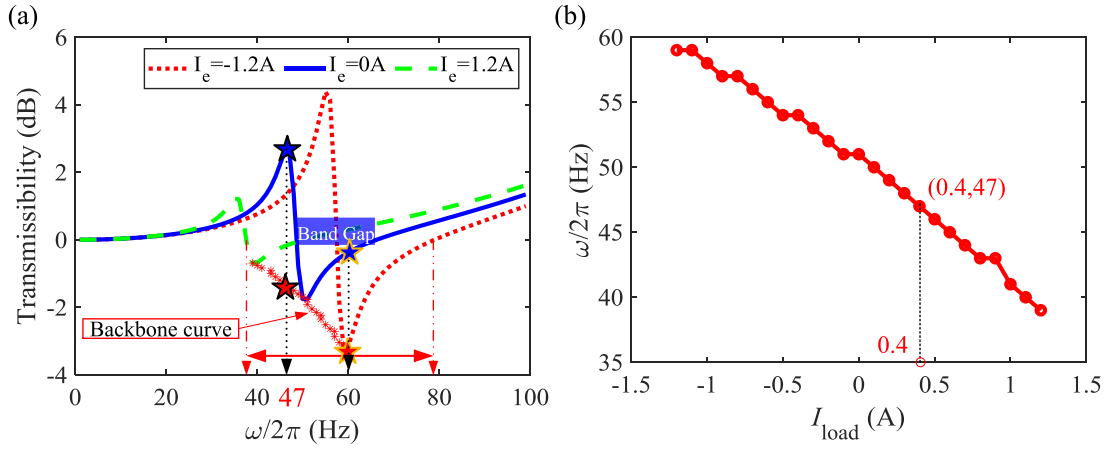

Fig. 10. (a) The comparison of the wave transmissibility when the load current is −1.2 A (red dotted line), 0 A (blue solid line) and 1.2 A (green dashed line). (b) The relation between the load current and the central frequency of the band gap. (For interpretation of the references to color in this figure legend, the reader is referred to the web version of this article.)

rewritten as

$$
\begin{aligned}
F_{\mathrm{SA-QZS}}(x_j,t) = k_{\mathrm{v}}&\left[z_j(t)-\sum_{k=1}^{K}\phi_s(x_j)p_s(t)\right]\\
&-\Gamma_1\left[z_j(t)-\sum_{k=1}^{K}\phi_s(x_j)p_s(t)\right]-\Gamma_2\left[z_j(t)-\sum_{k=1}^{K}\phi_s(x_j)p_s(t)\right]^3\\
&-\Gamma_3\left[z_j(t)-\sum_{k=1}^{K}\phi_s(x_j)p_s(t)\right]^5-\Gamma_4\left[z_j(t)-\sum_{k=1}^{K}\phi_s(x_j)p_s(t)\right]^7\\
&-\frac{\sigma^2(2r+2l+g)}{2\mu_0}\left[2\hbar\left(z_j(t)-\sum_{k=1}^{K}\phi_s(x_j)p_s(t)\right)\right.\\
&\left.-\hbar\left(z_j(t)-\sum_{k=1}^{K}\phi_k(x_j)p_k(t)+h\right)-\hbar\left(z_j(t)-\sum_{k=1}^{K}\phi_k(x_j)p_k(t)+h\right)\right]
\end{aligned}
\tag{41}
$$

where Γ_1, Γ_2, Γ_3 and Γ_4 are fitted coefficients obtained by utilizing MATLAB® function *lsqcurvefit* based on the trust-region-reflective algorithm.

The comparison between the exact electromagnetic force of the RM and the approximate one is presented in Fig. 9(a), when the load current is 1.2 A. The error of the fitted electromagnetic force is given in Fig. 9(b). From Fig. 9(a) and (b), it is evident that the maximum absolute error between the exact electromagnetic force and the approximate one is below 0.08 N, which indicates that the approximate expression matches well with the exact one in the displacement range from −10 mm to 10 mm. Therefore, the fitted expression can be employed to conduct the analysis of wave propagations alone the semi-active meta-beam.

The wave transmissibility of the semi-active meta-beam is depicted in Fig. 10(a) in which the green dashed line, blue solid line and red dotted line correspond to the load current of −1.2A, 0A and 1.2A, respectively. The air gap between the inner and outer magnet rings is 5 mm. In the absence of the load current, the RM does not work, and the central frequency of the band gap of the traditional HSLDS resonators is about 50 Hz. Given a positive load current, the semi-active meta-beam can attenuate the elastic wave in a much lower frequency range, compared with the traditional meta-beam, suggesting that a positive current helps lower the band gap further. Instead, the elastic wave could be attenuated in a higher frequency range when the load current is −1.2 A. Namely, the band gap is shifted to a high frequency range when a negative load current is applied on the coil.

From Fig. 10, one can see that the band gap of the semi-active meta-beam ranges from 38 Hz to 80 Hz when the load current is limited in the range [−1.2A, 1.2A]. The transmissibility at the central frequency for different load currents is denoted by a series of asterisks in Fig. 10(a), which form a backbone curve of transmissibility from 39 Hz and 60 Hz for the semi-active meta-beam. In addition, in the frequency range from 60 Hz to 80 Hz, the transmissibility is determined by the semi-active meta-beam with load current −1.2 A, as shown in the red dotted line. In order to unravel the effect of the load current on the central frequency clearly, Fig. 10(b) depicts the variation of the central frequency with respect to load current. Obviously, with the increase of the load current, the central frequency of the band gap decreases almost linearly, consistent with the theoretical analysis presented in Fig. 6.

4.4. Wave characteristics of the semi-active meta-beam

In order to validate the effect of load current on wave attenuation, two excitation frequencies (47 Hz and 60 Hz) are selected to delineate the displacement response of the meta-beam. At 47 Hz, which is close to the resonant frequency of the traditional HSLDS resonators, the wave

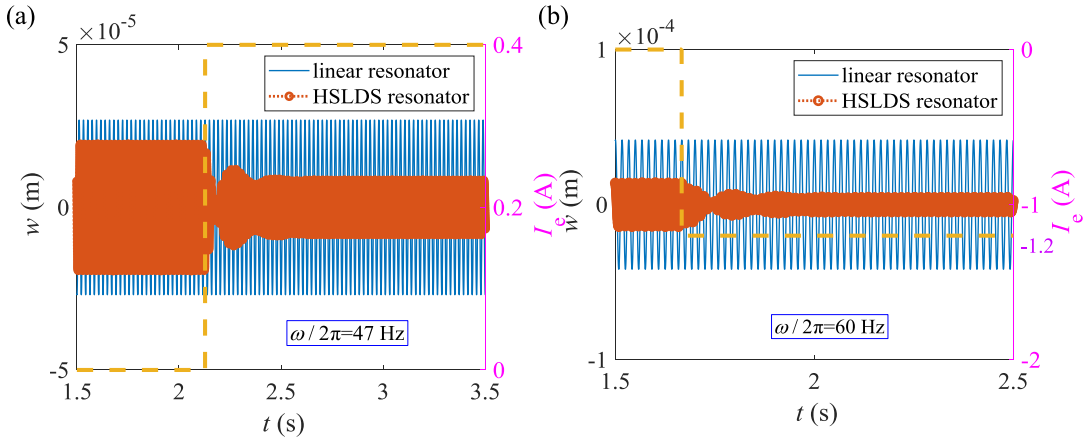

Fig. 11. Responses of the semi-active meta-beam at the right-hand side when the external frequency is (a) 47 Hz and (b) 60 Hz. The blue solid line and the orange dotted line with circles denote the meta-beam with linear resonators and semi-active QZS resonators, respectively.

transmissibility of the passive meta-beam and the semi-active meta-beam are marked by blue and red five-pointed stars with black edge, respectively, in Fig. 10(a). The corresponding displacement responses of the meta-beam are illustrated in Fig. 11(a), where the blue solid line and orange dotted line with circles denote the meta-beam with linear resonators and HSLDS resonators, respectively. Note that, the linear resonator is constructed by removing both the NSM and RM and only keeping a linear spring and a mass, and the passive HSLDS resonator can be switched to a semi-active one when the load current acts on the coil.

As shown in Fig. 11(a), the displacement response of the meta-beam can be divided into two time segments by a demarcating time $t = 2.13$ s for the case of 47 Hz. In the first segment, $t<2.13$ s, the load current is zero, and then the semi-active QZS resonator degrades into a passive one. Nevertheless, the displacement amplitude of the meta-beam with passive HSLDS resonators is smaller than that of the meta-beam with linear resonators. At $t = 2.13$ s, a load current of $I_{\text{load}} = 0.4$A is deployed, and the meta-beam is switched to a semi-active one. After about 0.3 s, the transient displacement response fades away. Clearly, the displacement amplitude of the meta-beam with semi-active QZS resonators ($t \geq 2.13$s) is about a half of that of the meta-beam with passive QZS resonators ($t < 2.13$s), and also much smaller than that of the meta-beam with linear resonators.

For 60 Hz case (larger than the central frequency of the band gap of the traditional meta-beam), the wave transmissibility of the meta-beam is marked by blue and red five-pointed stars with golden edge in Fig. 10(a). The displacement response of the meta-beam corresponding to the marked point is shown in Fig. 11(b). Clearly, the displacement response shows the same trend as the one observed at 47 Hz. In the first segment of $t<1.67$ s, the displacement amplitude of the meta-beam with passive HSLDS resonators is smaller than that with linear resonators. Upon the deployment of a load current of −1.2 A at $t = 1.67$ s, the meta-beam is switched into a semi-active one, and the displacement amplitude is substantially reduced.

5. Conclusions

This paper proposes a semi-active quasi-zero-stiffness (QZS) resonator by introducing a regulatory mechanism (RM) into a conventional HSLDS resonator. The HSLDS resonator is formed by combining a linear spring and a pair of magnet rings (negative-stiffness mechanism), and the RM is constructed by an electrically charged coil and a permanent magnet ring. The static analysis of the semi-active resonator shows that the stiffness of the semi-active QZS resonator can be effectively neutralized by the negative-stiffness mechanism (NSM). More importantly, the stiffness can be adjusted by the RM, which is a more intriguing feature compared with that of the traditional HSLDS resonator.

Attaching the semi-active resonators onto a beam periodically, a semi-active meta-beam is realized. Using the transfer matrix method, the dispersion relation and the band structure of the semi-active meta-beam are scrutinized. By solving the equation of motion of the semi-active meta-beam and calculating the wave transmissibility, the analytical band structure is validated numerically. Both the analytical and the numerical results show that the band gap can be effectively shifted to a low frequency range due to the NSM. More importantly, the passive HSLDS resonator can be switched into a semi-active one through the deployment of a load current on the coil. This results in a substantial broadening of the band gap, thus providing an alternative way to overcome the intrinsic limitation of conventional passive local-resonance-based methods in terms of achieving broad bandwidth.

Declaration of Competing Interests

The authors declare that they have no known competing financial interests or personal relationships that could have appeared to influence the work reported in this paper.

CRediT authorship contribution statement

Kai Wang: Conceptualization, Methodology, Software, Writing - original draft. **Jiaxi Zhou:** Resources, Investigation, Data curation, Writing - review & editing. **Huajiang Ouyang:** Resources, Data curation, Writing - review & editing. **Li Cheng:** Writing - review & editing. **Daolin Xu:** Supervision.

Acknowledgments

This research work was supported by National Key R&D Program of China (2017YFB1102801), National Natural Science Foundation of China (11972152, 11572116) and the Laboratory of Science and Technology on Integrated Logistics Support. The First author, Kai Wang, would like to thank the support from the China Scholarship Council (CSC) which sponsors his visit to the University of Liverpool.

References

[1] Ma G, Sheng P. Acoustic metamaterials: from local resonances to broad horizons. Sci Adv 2016;2:e1501595.
[2] Khelif A, Choujaa A, Benchabane S, Djafari-Rouhani B, Laude V. Guiding and bending of acoustic waves in highly confined phononic crystal waveguides. Appl Phys Lett 2004;84:4400–2. doi:10.1063/1.1757642.
[3] Morvaridi M, Carta G, Brun M. Platonic crystal with low-frequency locally-resonant spiral structures: wave trapping, transmission amplification, shielding and edge waves. J Mech Phys Solids 2018;121:496–516. doi:10.1016/j.jmps.2018.08.017.

[4] Mei J, Ma G, Yang M, Yang Z, Wen W, Sheng P. Dark acoustic metamaterials as super absorbers for low-frequency sound. Nat Commun 2012;3:756–7. doi:10.1038/ncomms1758.
[5] Wang K, Zhou J, Daolin X, Ouyang H. Tunable low-frequency torsional-wave band gaps in a meta-shaft. J Phys D Appl Phys 2019;52:055104 http://iopscience.iop.org/. doi:10.1088/1361-6463/aaf039.
[6] Elnady T, Elsabbagh A, Akl W, Mohamady O, Garcia-Chocano VM, Torrent D, et al. Quenching of acoustic bandgaps by flow noise. Appl Phys Lett 2009;94:2007–10. doi:10.1063/1.3111797.
[7] Xiang HJ, Shi ZF, Wang SJ, Mo YL. Periodic materials-based vibration attenuation in layered foundations: experimental validation. Smart Mater Struct 2012;21:112003. doi:10.1088/0964-1726/21/11/112003.
[8] Huang Y, Li J, Chen W, Bao R. Tunable bandgaps in soft phononic plates with spring-mass-like resonators. Int J Mech Sci 2019;151:300–13. doi:10.1016/j.ijmecsci.2018.11.029.
[9] Matlack KH, Bauhofer A, Krödel S, Palermo A, Daraio C. Composite 3D-printed metastructures for low frequency and broadband vibration absorption. Proc Natl Acad Sci U S A 2016;113:8386–90. doi:10.1073/pnas.1600171113.
[10] Rothos VM, Vakakis AF. Dynamic interactions of traveling waves propagating in a linear chain with an local essentially nonlinear attachment. Wave Motion 2009;46:174–88. doi:10.1016/j.wavemoti.2008.10.004.
[11] Wang K, Zhou J, Xu D, Ouyang H. Lower band gaps of longitudinal wave in a one-dimensional periodic rod by exploiting geometrical nonlinearity. Mech Syst Signal Process 2019;124:664–78. doi:10.1016/j.ymssp.2019.02.008.
[12] Yu D, Liu Y, Zhao H, Wang G, Qiu J. Flexural vibration band gaps in Euler–Bernoulli beams with locally resonant structures with two degrees of freedom. Phys Rev B 2006;73:064301. doi:10.1103/PhysRevB.73.064301.
[13] Xu X, Barnhart M V, Fang X, Wen J, Chen Y, Huang G. A nonlinear dissipative elastic metamaterial for broadband wave mitigation. Int J Mech Sci 2019;164:105159. doi:10.1016/j.ijmecsci.2019.105159.
[14] Qian YJ, Cui QD, Yang XD, Zhang W. Manipulating transverse waves through 1D metamaterial by longitudinal vibrations. Int J Mech Sci 2020;168:105296. doi:10.1016/j.ijmecsci.2019.105296.
[15] Cai C, Zhou J, Wu L, Wang K, Xu D, Ouyang H. Design and numerical validation of quasi-zero-stiffness metamaterials for very low-frequency band gaps. Compos Struct 2020;236:111862. doi:10.1016/j.compstruct.2020.111862.
[16] Wang K, Zhou J, Cai C, Xu D, Ouyang H. Mathematical modeling and analysis of a meta-plate for very low-frequency band gap. Appl Math Model 2019;73:581–97. doi:10.1016/j.apm.2019.04.033.
[17] Zhou W, Su Y, Muhammad Chen W, Lim CW. Voltage-controlled quantum valley hall effect in dielectric membrane-type acoustic metamaterials. Int J Mech Sci 2019;172:105368. doi:10.1016/j.ijmecsci.2019.105368.
[18] Zhang K, Zhao P, Hong F, Yu Y, Deng Z. On the directional wave propagation in the tetrachiral and hexachiral lattices with local resonators. Smart Mater Struct 2020;29:015017. doi:10.1088/1361-665x/ab5764.
[19] Liu Z, Zhang X, Mao Y, Zhu YY, Yang Z, Chan CT, et al. Locally resonant sonic materials. Science 2000;289(80–):1734–6. doi:10.1126/science.289.5485.1734.
[20] D'Alessandro L, Ardito R, Braghin F, Corigliano A. Low frequency 3D ultra-wide vibration attenuation via elastic metamaterial. Sci Rep 2019;9:8039. doi:10.1038/s41598-019-44507-6.
[21] Pai PF, Peng H, Jiang S. Acoustic metamaterial beams based on multi-frequency vibration absorbers. Int J Mech Sci 2014;79:195–205. doi:10.1016/j.ijmecsci.2013.12.013.
[22] Wen S, Xiong Y, Hao S, Li F, Zhang C. Enhanced band-gap properties of an acoustic metamaterial beam with periodically variable cross-sections. Int J Mech Sci 2020;166. doi:10.1016/j.ijmecsci.2019.105229.
[23] Xiao Y, Wen J, Huang L, Wen X. Analysis and experimental realization of locally resonant phononic plates carrying a periodic array of beam-like resonators. J Phys D Appl Phys 2014;47:045307. doi:10.1088/0022-3727/47/4/045307.
[24] Wang YF, Wang YS, Laude V. Wave propagation in two-dimensional viscoelastic metamaterials. Phys Rev B 2015;92:104110. doi:10.1103/PhysRevB.92.104110.
[25] Yu D, Liu Y, Wang G, Cai L, Qiu J. Low frequency torsional vibration gaps in the shaft with locally resonant structures. Phys Lett Sect A Gen At Solid State Phys 2006;348:410–15. doi:10.1016/j.physleta.2005.08.067.
[26] Wang G, Chen S, Wen J. Low-frequency locally resonant band gaps induced by arrays of resonant shunts with Antoniou's circuit: experimental investigation on beams. Smart Mater Struct 2011;20:015026. doi:10.1088/0964-1726/20/1/015026.
[27] Zhang S, Hui Wu J, Hu Z. Low-frequency locally resonant band-gaps in phononic crystal plates with periodic spiral resonators. J Appl Phys 2013;113:163511. doi:10.1063/1.4803075.
[28] Fang X, Wen J, Bonello B, Yin J, Yu D. Ultra-low and ultra-broadband nonlinear acoustic metamaterials. Nat Commun 2017;8:1–11. doi:10.1038/s41467-017-00671-9.
[29] Zhou J, Wang K, Xu D, Ouyang H. Local resonator with high-static-low-dynamic stiffness for lowering band gaps of flexural wave in beams. J Appl Phys 2017;121:044902. doi:10.1063/1.4974299.
[30] Wang K, Zhou J, Wang Q, Ouyang H, Xu D. Low-frequency band gaps in a metamaterial rod by negative-stiffness mechanisms : design and experimental validation. Appl Phys Lett 2019;114:251902. doi:10.1063/1.5099425.
[31] Li S, Dou Y, Chen T, Xu J, Li B, Zhang F. Designing a broad locally-resonant bandgap in a phononic crystals. Phys Lett Sect A Gen At Solid State Phys 2019;383:1371–7. doi:10.1016/j.physleta.2019.01.061.
[32] Fang X, Wen J, Yin J, Yu D, Xiao Y. Broadband and tunable one-dimensional strongly nonlinear acoustic metamaterials: theoretical study. Phys Rev E 2016;94:1–10. doi:10.1103/PhysRevE.94.052206.
[33] Fang X, Wen J, Yu D, Yin J. Bridging-Coupling band gaps in nonlinear acoustic metamaterials. Phys Rev Appl 2018;10:054049. doi:10.1103/PhysRevApplied.10.054049.
[34] Liu C, Reina C. Broadband locally resonant metamaterials with graded hierarchical architecture. J Appl Phys 2018;123:095108. doi:10.1063/1.5003264.
[35] Celli P, Yousefzadeh B, Daraio C, Gonella S. Bandgap widening by disorder in rainbow metamaterials. Appl Phys Lett 2019;114:091903. doi:10.1063/1.5081916.
[36] Xiao Y, Wen J, Wen X. Broadband locally resonant beams containing multiple periodic arrays of attached resonators. Phys Lett Sect A Gen At Solid State Phys 2012;376:1384–90. doi:10.1016/j.physleta.2012.02.059.
[37] Zhou J, Wang K, Xu D, Ouyang H. Multi-low-frequency flexural wave attenuation in Euler–Bernoulli beams using local resonators containing negative-stiffness mechanisms. Phys Lett Sect A Gen At Solid State Phys 2017;381:3141–8. doi:10.1016/j.physleta.2017.08.020.
[38] Yang M, Sheng P. Sound absorption structures: from porous media to acoustic metamaterials. Annu Rev Mater Res 2017;47:83–114. doi:10.1146/annurev–matsci-070616-124032.
[39] Taniker S, Yilmaz C. Generating ultra wide vibration stop bands by a novel inertial amplification mechanism topology with flexure hinges. Int J Solids Struct 2017;106–107:129–38. doi:10.1016/j.ijsolstr.2016.11.026.
[40] Zhou J, Lingling D, Wang K, Xu D, Ouyang H. A nonlinear resonator with inertial amplification for very low-frequency flexural wave attenuations in beams. Nonlinear Dyn 2019;96:647–65. doi:10.1007/s11071-019-04812-1.
[41] Chen S, Fan Y, Fu Q, Wu H, Jin Y, Zheng J, et al. A review of tunable acoustic metamaterials. Appl Sci 2018;8:1480. doi:10.3390/app8091480.
[42] Chen Y, Huang G. An adaptive metamaterial beam with hybrid shunting circuits for extremely broadband control of flexural wave (Conference presentation). Smart Mater Struct 2016;25:105036. doi:10.1117/12.2259785.
[43] Yi K, Ouisse M, Sadoulet-Reboul E, Matten G. Active metamaterials with broadband controllable stiffness for tunable band gaps and non-reciprocal wave propagation. Smart Mater Struct 2019;28:065025. doi:10.1088/1361-665x/ab19dc.
[44] Sirota L, Semperlotti F, Annaswamy AM. Tunable and reconfigurable mechanical transmission-line metamaterials via direct active feedback control. Mech Syst Signal Process 2019;123:117–30.
[45] Sang S, Mhannawee A, Wang Z. A design of active elastic metamaterials with negative mass density and tunable bulk modulus. Acta Mech 2019;230:1003–8. doi:10.1007/s00707-018-2320-2.
[46] Wang Z, Zhang Q, Zhang K, Hu G. Tunable digital metamaterial for broadband vibration isolation at low frequency. Adv Mater 2016;28:9857–61. doi:10.1002/adma.201604009.
[47] Zhang Q, Zhang K, Hu G. Tunable fluid-solid metamaterials for manipulation of elastic wave propagation in broad frequency range. Appl Phys Lett 2018;112:221906. doi:10.1063/1.5023307.
[48] De Sousa VC, Tan D, De Marqui C, Erturk A. Tunable metamaterial beam with shape memory alloy resonators: theory and experiment. Appl Phys Lett 2018;113:143502. doi:10.1063/1.5050213.
[49] Shiri A, Shoulaie A. A new methodology for magnetic force calculations between planar spiral coils. Prog Electromagn Res 2009;95:39–57.
[50] Pu H, Yuan S, Peng Y, Meng K, Zhao J, Xie R, et al. Multi-layer electromagnetic spring with tunable negative stiffness for semi-active vibration isolation. Mech Syst Signal Process 2019;121:942–60. doi:10.1016/j.ymssp.2018.12.028.
[51] Zhou J, Wang K, Xu D, Ouyang H, Fu Y. Vibration isolation in neonatal transport by using a quasi-zero-stiffness isolator. J Vib Control 2018;24:3278–91. doi:10.1177/1077546317703866.
[52] Cao Q, Wiercigroch M, Pavlovskaia EE, Thompson JM, Grebogi C. Piecewise linear approach to an archetypal oscillator for smooth and discontinuous dynamics. Philos Trans A Math Phys Eng Sci 2008;366:635–52. doi:10.1098/rsta.2007.2115.
[53] Hao Z, Cao Q, Wiercigroch M. Nonlinear dynamics of the quasi-zero-stiffness SD oscillator based upon the local and global bifurcation analyses. Nonlinear Dyn 2017;87:987–1014. doi:10.1007/s11071-016-3093-6.